Columnar-to-equiaxed transition in a laser scan for metal additive manufacturing

To cite this article: L Yuan *et al* 2020 *IOP Conf. Ser.: Mater. Sci. Eng.* **861** 012007

View the article online for updates and enhancements.

Columnar-to-equiaxed transition in a laser scan for metal additive manufacturing*

L Yuan[1], A S Sabau[2], D StJohn[3], A Prasad[3] and P D Lee[4]

[1] University of South Carolina, Columbia, SC, 29201, US
[2] Oak Ridge National Laboratory, Oak Ridge, TN 37830, US
[3] The University of Queensland, St Lucia QLD 4072, Australia
[4] University College London, London WC1E 6BT, UK

E-mail: langyuan@cec.sc.edu

Abstract. In laser powder bed fusion additive manufacturing (LPBFAM), different solidification conditions, e.g., thermal gradient and cooling rate, can be achieved by controlling the process parameters, such as laser power and laser speed. Tailoring the behaviour of the columnar to equiaxed transition (CET) of the printed alloy during fabrication can facilitate the production of highly customized microstructures. In this study, effective analytical solutions for both thermal conduction and solidification are employed to model solidifying melt pools. Microstructure textures and solidification conditions are evaluated for numerous combinations of laser power and laser speed under bead-on-plate conditions. This analytical-based high-throughput tool was demonstrated to select specific process parameters that lead to desired microstructures. Two selected process conditions were examined in detail by a highly parallelized microstructural solidification model to reveal both nucleation and grain growth. Both numerical solutions agree well with experiments that are performed based on bead-on-plate conditions, indicating that these numerical models aid evaluation of the nucleation parameters, providing insights for controlling CET during the LPBFAM processing.

1. Introduction

The Laser Powder Bed Fusion Additive Manufacturing process (LPBFAM) is one of the most used additive manufacturing processes for direct materials consolidation. One of the major advantages is that process parameters, e.g. laser power, speed, spot size and scanning paths and build plate temperature, can be adjusted locally over wide ranges independently, leading to dramatically different solidification conditions, e.g. thermal gradient and solidification speed. In turn, tailoring the solidification environment can result in location specific microstructures, thus, customized material properties for optimal performance [1–3].

Effectively controlling the columnar to equiaxed transition (CET) is one of the basic requirements to fabricate materials with deliberate microstructures. Although CET has been well studied for solidification processes, to eliminate columnar grains and promote equiaxed grains in metal additive

manufacturing (AM) is rather challenging. In the melt pool, columnar grains typically form on account of the prevailing local directional solidification conditions, where grains grow epitaxially from the preexisting grains with no energy barrier for nucleation. Means to promote CET during AM can be generally attributed to the following four catagories:1) control process parameters [4, 5]; 2) modify alloy composition [6]; 3) add nano/micro particles [7, 8]; and 4) interact with external fields [9, 10]. Recent research through both numerical analysis [4] and experimental observations [11] shows that thermal conditions via controlling process parameters nevertheless play an important role to facilitate other factors, such as variation of alloy composition and grain refiner, to promote nucleation. Due to high computational cost for physics-based numerical models, an effective means based on analytical solutions that can correlate solidification conditions from a wide range of process parameters to CET is preferred to assist the selection of process conditions for desired microstructure morphologies.

Classic solidification theory suggests that sufficient constitutional supercooling (CS) ahead of the solidification front is required to activate potent heterogenous nucleant particles, which essentially triggers a nucleation event, eventually resulting in CET. Among the theories, the Interdependence Model describes the establishment of Nucleation Free Zone (NFZ) due to the existence of CS whose length governs the distance at which a new nucleation event is triggered. On this basis, the model predicts the average grain size based on the location of the next nucleation event [12, 13]. This model has also been successfully applied to understand the grain refinement during AM [11]. To theoretically predict the CET, the analytical solution proposed by Hunt [14] has been widely adopted to generate the CET map based on thermal gradient and solidification speed [15]. Gaumann *et al.* extended Hunt's model with the Kurz–Giovanola–Trivedi (KGT) model to account for rapid solidification and applied it to achieve single crystals during a laser deposition process [16].

In this study, analytical solutions for both temperature and CET are resolved to effectively screen a wide range of laser process parameters, namely, laser power and laser speed, for bead-on-plate conditions during the LPBFAM process. The selection of bead-on-plate conditions is due to its simplicity and the identical solidification principle during the fabrication process. A process map based on the predictions is generated to guide the experimental design. To further evaluate the predictions, selective process parameters that result in different grain morphologies are predicted by a highly parallelized microstructural solidification model to reveal both nucleation and grain growth. Predictions from both methods are compared with experiments, providing effective tools to examine CET during LPBFAM processing.

2. Model description

Analytical solutions have been widely applied to evaluate process conditions and microstructure morphologies during solidification processes. They are effective methods to screen a large range of process parameters in comparison to physics-based high-fidelity numerical models. With necessary calibrations, they can provide acceptable accuracy that reflects the general material's behavior. Two analytical solutions for the temperature profile in a moving distributed heat source and the CET event, respectively, are implemented here to assess process conditions. Meanwhile, to examine details about the solidification microstructures, a highly parallel solidification model was integrated with the thermal analytical solutions to predict the nucleation events and grain growth. A summary of both analytical solutions and the solidification model is provided below.

2.1. Analytical solutions

Assuming only heat conduction occurs during laser scanning, a steady-state temperature profile can be reached for a moving heat source. Rosenthal has provided a solution for a moving point heat source [17]. For a Gaussian laser beam, the distribution of laser intensity is described as:

$$q(r) = \frac{2AP}{\pi R^2} \exp\left(-\frac{2r^2}{R^2}\right) \tag{1}$$

where P is the laser power, A is the laser absorption coefficient, R is the laser beam radius and r is the distance to the laser center. By integrating the heat flux based on the distributed heat source on the

surface of a semi-infinite plate and assuming the laser is moving along the x direction, the temperature profile at quasi-steady state can be expressed as [17, 18]:

$$T(x,y,z) = T_0 + \frac{2AP}{\pi^{1.5}\rho c_p} \times \frac{\int_0^\infty \exp\left(-\frac{2(x+Vt)^2 + 2y^2}{R^2 + 8\alpha t} - \frac{z^2}{4\alpha t}\right)}{\sqrt{\alpha t}(R^2 + 8\alpha t)} dt \qquad (2)$$

where (x,y,z) is the location coordinate relative to the heat source, T_0 is the build plate temperature, ρ is the density, c_p is the specific heat, α is the thermal diffusivity, V is the laser speed and t is the time.

Equation (2) provides a 3D quasi-steady thermal profile within the melt pool. The solidification conditions, both thermal gradient and solidification rate, can be extracted for the prediction of CET. The extended model proposed by Gaumann *et al.* [16] is applied here to evaluate the thermal conditions. The dendrite tip velocity, *v,* is approximated by:

$$v = a\,(\Delta T)^n \qquad (3)$$

where a and n are alloy dependent constants. The fraction solid of equiaxed grains, ϕ_E, then, can be expressed as:

$$\phi_E = \frac{4\pi n_0}{3}\left(\frac{1}{G(n+1)}\left(1 - \frac{\Delta T^{n+1}}{\left(\frac{v}{a}\right)^{\frac{n+1}{n}}}\right)\left(\frac{v}{a}\right)^{\frac{1}{n}}\right)^3 \qquad (4)$$

where n_0 is the nucleation density, G is the thermal gradient, v is the solidification speed, ΔT is the tip undercooling. When $\phi_E < 0.0066$, the structure is fully columnar. When $\phi_E > 0.66$, a fully equiaxed structure is expected [14]. For solidification under a high temperature gradient, the nuclei density plays an important role and the nucleation undercooling can be safely neglected [16]. Therefore, equation (4) can be simplified to:

$$\frac{G^n}{v} = \frac{1}{a}\left(\frac{1}{n+1}\left(\frac{4\pi n_0}{3\phi_E}\right)^{\frac{1}{3}}\right)^n \qquad (5)$$

With given G and v, the higher the value obtained from equation (5), the easier the growth of columnar grains.

2.2. Solidification microstructure model

To predict the solidification microstructure based on thermal conditions, a parallel solidification code, adapted from the open source code μMatIC [19–21], was developed to predict the grain structure during rapid solidification. In this model, at every time step, the local quasi-steady temperature profiles are directly calculated from the thermal analytical solution and drive the nucleation event and grain growth. The code takes a master-worker approach, where a master node allocates subdomains to each worker (computational node) for heavy computation based on the status of the thermal profiles. For instance, if the temperature in the subdomain is fully solid or below the solidus temperature, no calculation will be assigned to workers to reduce both calculation time and memory burden. This allows a significant increase of computational efficiency for large geometries on high performance computers. In the model, the nucleation of new grains is modelled assuming a Gaussian distribution of nucleation density (n):

$$\frac{dn}{d(\Delta T)} = \frac{n_0}{\sqrt{2\pi}\sigma_n}\exp\left[-\frac{1}{2}\left(\frac{\Delta T - \Delta T_n}{\sigma_n}\right)^2\right] \qquad (6)$$

where σ_n is the standard deviation of the Gaussian distribution, ΔT_n is the mean nucleation undercooling. and grain growth is then simulated based on the modified KGT model according to [16] as shown in equation (3). The implementation details can be found in prior publications [19–21].

3. Results and discussion

The nickel-based superalloy, IN625, was studied both numerically and experimentally. The thermal analytical solution does not take into account the temperature dependent material properties nor the latent heat during solidification. As such, the material's properties and laser absorption coefficient were calibrated by comparing with bead-on-plate experiments in LPBFAM. In addition, only conditions where the laser operates in the conduction melting mode are considered. The applied simulation parameters and general process conditions are listed in table 1. Figure 1 shows the predicted thermal profiles and the melt pool size for 75W and 100mm/s laser conditions. Melt pool shape and the dimensions can be consistently repeated with the current set of parameters in comparison with experiments for views of both cross section and top surface (Note that figure 1(d) is the cross-section of the laser scan and shows the melt pool depth and width; figure 1(e) shows the top view at the end of laser scan which reveals the length and width of the melt pool). Note that the accuracy of the prediction may vary as the laser conditions change. However, the general behaviors of thermal conditions remain valid to evaluate the process conditions and the potency of the CET.
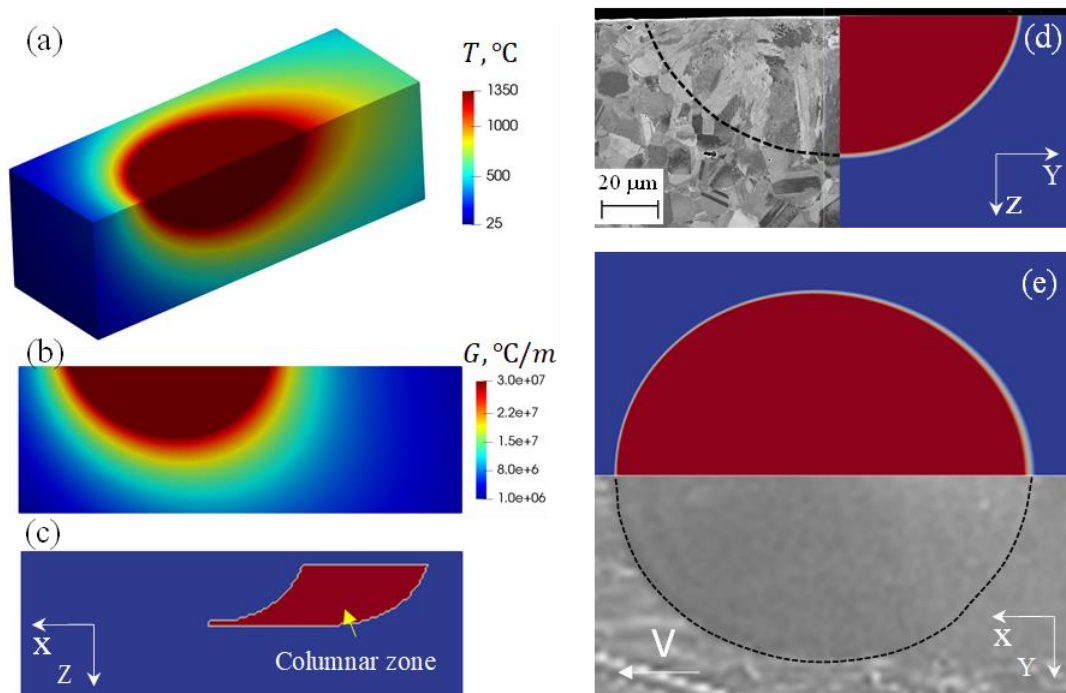
Figure 1. Analytical thermal predictions for laser parameters at 75W and 100mm/s: (a) steady state 3D thermal profiles; (b) thermal gradient at x-z cross section; (c) indication of CET; (d) comparison of melt pool size in the z-y direction; and (e) comparison of melt pool along the substrate surface where the laser was turned off.

Equation (5) was calculated based on the local G and v to estimate CET. To determine the tip growth velocity, v, both a and n are estimated by fitting equation (3) to the dendrite/cellular tip undercooling calculated with the Marginal Stability growth model [24]. Using the thermal dynamic data calculated by ThermoCalc to obtain the liquidus slopes and partitioning coefficients and assuming a constant Gibbs–Thomson coefficient of 1.0×10^{-7} m K and equal diffusion coefficients for the alloying elements of 3.0×10^{-9} m^2/s., a and n were calculated at 3.97×10^{-6}m/s°C$^{3.1}$ and 3.1, respectively. The detailed approach can be found in [25]. Since the nucleation density n_0 largely determines the critical value for CET, $n_0 = 2 \times 10^{15}$ m^{-3} was taken as a reference value to demonstrate the potential columnar zone, as shown in figure 1(c). Note that changing n_0 will change the size of columnar zone from the analytical solution. To effectively evaluate the solidification conditions for each case, average values for cooling rate, R, and G^n/v are calculated for the semisolid region located at the tail of the melt

pool (the region after the maximum depth). The values of two cases, P=75W, V=100mm/s and P=75W, V=500mm/s, are shown in table 2, together with measured average primary dendrite arm spacing (PDAS). Case 2 had a higher cooling rate and higher G^n/v value, indicating that it should yield(?) finer PDAS and higher potency to grow columnar grains. The microstructures from bead-on-plate experiments for both cases are shown in figure 2. Qualitatively, Case 2 showed less equiaxed zone in comparison with Case 1. In addition, by measuring the average PDAS, Case 2 had the average value of 0.38 μm while Case 1 was 0.68 μm. The analytical predictions are consistent with experimental observations.

Table 1. Simulation Parameters for IN625[22, 23]

Parameter	Unit	Value
Density, ρ	kg/m^3	8440
Specific heat, c_p	J/kg/ ℃	600
Liquidus temperature, T_{sol}	℃	1290
Liquidus temperature, T_{liq}	℃	1350
Thermal diffusivity, α	m^2/s	4.94e-6
Laser absorption coefficient, A		0.33
Laser beam radius, R	mm	0.05
Build plate temperature, T_0	℃	25

Table 2. Representative values from the analytical solutions

|	P, W	V, mm/s	R_{avg}, K/s	G^n/v	PDAS_Exp, μm
Case 1	75	100	1.02×10^6	6.66×10^{26}	0.68±0.07
Case 2	75	500	5.47×10^6	2.43×10^{27}	0.38±0.06
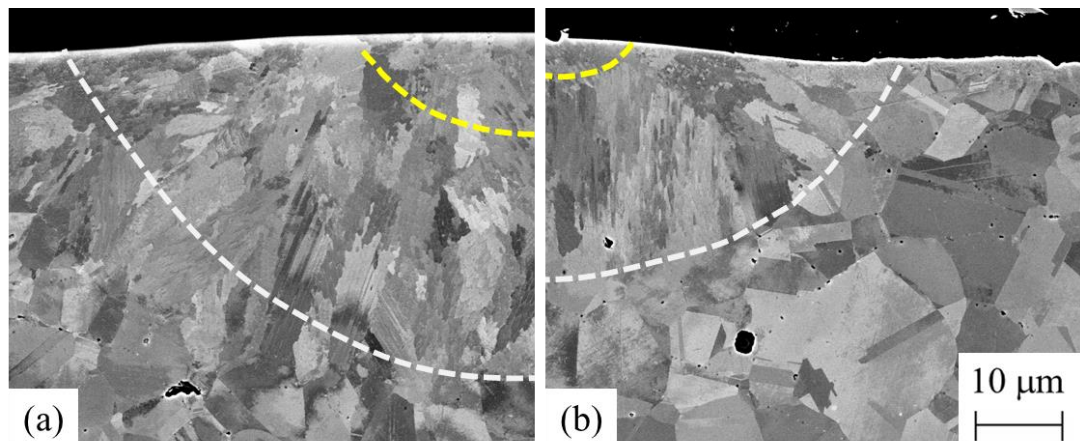
Figure 2. Microstructures at the y-z cross-section for (a) Case 1: P=75W, V=100mm/s; and (b) Case 2: P=75W, V=500mm/s. Within the melt pool, the top line indicates the CET line and the bottom line indicates the melt pool boundary.

Based on the average R and G^n/v values, a wide range of process parameters can be examined. Assuming both laser power and speed can vary from 50W to 500W and from 0.05 m/s to 2 m/s, respectively, a design of experiment was performed based on the Latin Hypercube sampling method [26] to fill the parametrical space. To avoid both insufficient melting and keyholing [27], the correlation of P and V were constrained by:

$$100 < \frac{P}{\sqrt{V}} < 350 \qquad (7)$$

Both the lower and upper bounds in equation (7) were determined by bead-on-plate experiments on IN625. The combinations of P and V are shown in figure 3(a), which includes 270 different process conditions. The average R and G^n/v, calculated from the analytical solutions, is then displayed in figure 3(b). The R and G^n/v map will assist the selection of process conditions for potentially different solidification features. For example, to produce potential columnar grains structures with less residual stress or with less potency to solidification cracking, process conditions with high G^n/v values and low cooling rate are preferred, respectively. In figure 3(b), the conditions located in left-upper corner most likely can satisfy the requirements. By selecting the $\log_{10}(G^n/v)$ value of 26.5 and average cooling rate of $2.5 \times 10^6 \; ^\circ C/s$ as the lower bounds, the conditions are highlighted as boxed dots in figure 3(a), which can be used to specify the experimental conditions.
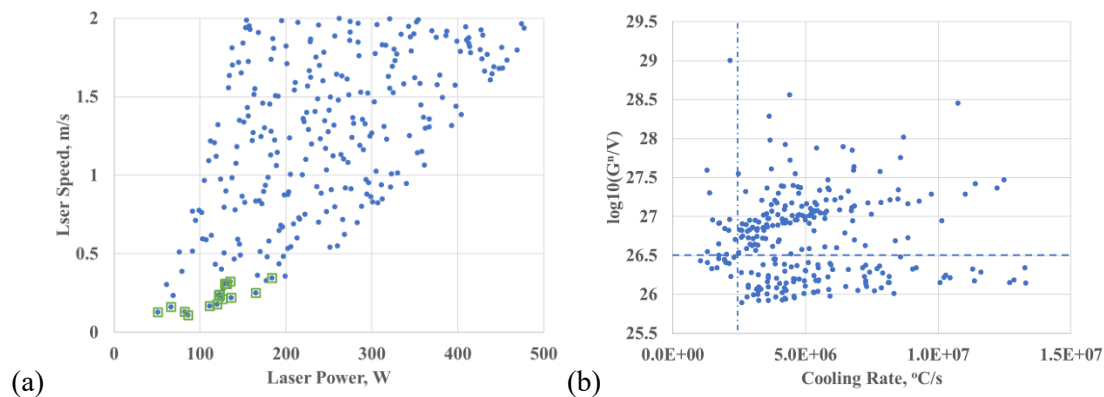
Figure 3. (a) Design of Experiment for laser power and laser speed: the boxed dots indicate the conditions with low average cooling rate and low CET potency. (b) Distribution based on average cooling rate and G^n/v.

Both cases in table 2 were simulated by the solidification microstructure model using the temperature profiles calculated by the analytical solution. In the current simulation mode, segregation information is neglected. Therefore, only thermal undercooling drives the nucleation and growth. A grid size of $2.5 \times 10^{-7} m$ was chosen based on the PDAS. The selection of the nucleation parameters will determine the morphologies and size of the grain. Since the relative observations between the two cases were of interest in the current study, a nucleation undercooling of $10 \; ^\circ C$ with standard deviation of $2 \; ^\circ C$ and a maximum nucleation density of 1×10^{17} were used for both simulations. The calculation domain was set as a cube with a length of 5.0×10^{-5} m, which covered the entire melt pool for the display of the steady state grain structures. To mimic the initial grain conditions, the domain starts with fine grains. As the laser scanned and melted the substrate, remelting and solidification would occur to form the final microstructures. The predicted grain structures are shown in figure 4.
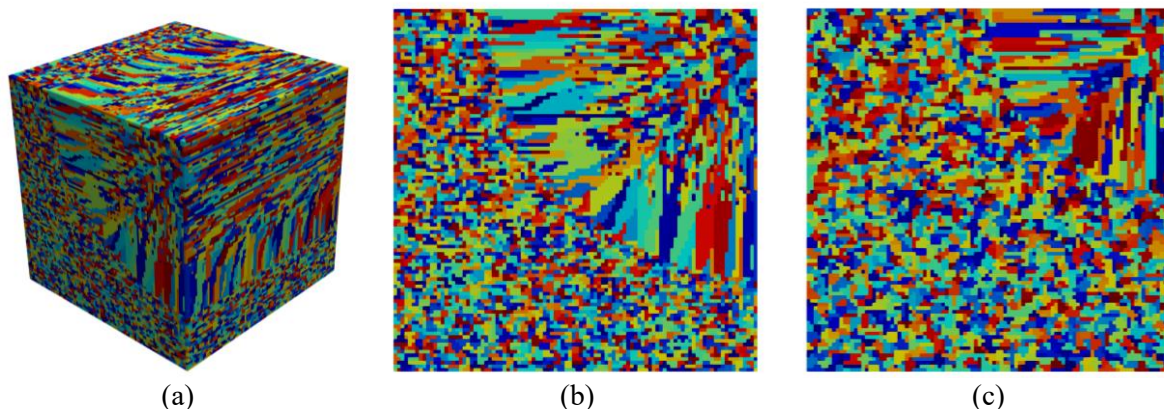
Figure 4. Predicted grain structures: (a) 3D view for Case 1: P=75W; V=100mm/s; (b) y-z cross-sectional view for Case 1; (c) y-z cross-sectional view for Case 2: P=75W, V=500mm/s.

With the current set of simulation parameters, the results reflect the general trend as shown in figure 2 that Case 1 tends to have a larger nucleation zone. Epitaxial growth dominates the bottom of the melt pool, where the columnar grains grow from the original fine grains.

High thermal gradients and high cooling rates are expected in the LPBFAM process. As shown in figure 5, following the Interdependence Model, with increasing thermal gradient, the magnitude of the constitutional supercooling is largely suppressed in terms of the Interdependence Model, shown in figure 5(a) by the maximum difference between T_E (the equilibrium temperature) and T_{A_highG} (actual temperature with high thermal gradient). With a high cooling rate, both the segregation and diffusion length of the solute are compressed, as shown in figure 5(b). The contribution of CS for nucleation may be neglected, where thermal supercooling dominates the solidification process. This also explains that columnar grains are preferred at the bottom of the melt pool besides epitaxial growth, where there is insufficient undercooling for nucleation at the initial stage of solidification. Therefore, limiting thermal gradient and grain growth speed will benefit nucleation, and in turn, facilitate the formation of equiaxed grains. The further development and implementation of the current solidification model can physically evaluate the theorical predictions and provide insights to the CET formation.
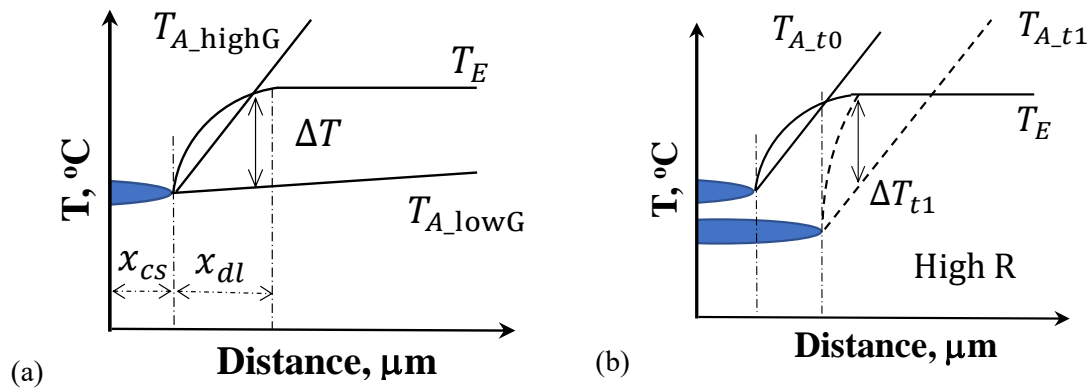
Figure 5. Schematic representation of the constitutionally supercooled zone as described by the Interdependence model: (a) with low and high thermal gradients; and (b) with high cooling rate at two time steps, $t0$ and $t1$.

4. Conclusions

Analytical solutions for both thermal conduction and solidification are applied to a broad range of laser power and speed on bead-on-plate conditions during LPBFAM. The average cooling rate, R and the CET criteria based on G^n/v are calculated for the solidifying region to evaluate the microstructure's texture. Qualitatively, the analytical solutions match experimental observations with necessary calibrations with the material properties. By combining different R and G^n/v, the process conditions that produce the desired grain size, morphology and potential defects can be selected. The extension of such a high throughput toolset provides effective means to examine full sets of key process parameters, including laser spot size, scanning paths and substrate temperature, to guide experimental design and locally control microstructure morphology.

Numerical simulations for two process conditions that generate different grain structures are simulated by a highly parallel microstructural solidification model to reveal both nucleation and grain growth. The predictions reflect the general solidification behaviours, as shown in the experiments with identical conditions, during solidification with both high thermal gradient and high cooling rate. The Interdependence Model suggests that thermal supercooling dominates the nucleation behaviour. Although the microstructure model did not include the alloy composition directly, it can be a valuable tool to directly examine process conditions and nucleation behaviours to guide design the microstructure.

References
[1]   DebRoy T *et al.* 2018 *Prog. Mater. Sci.* **92** 112–224
[2]   Bourell D L 2016 *Annu. Rev. Mater. Res.* **46** 1–18
[3]   Gu D D, Meiners W, Wissenbach K and Poprawe R 2012 *Int. Mater. Rev.* **57** 133–64
[4]   Haines M, Plotkowski A, Frederick C L, Schwalbach E J and Babu S S 2018 *Comput. Mater. Sci.* **155** 340–9
[5]   Liang Y-J, Cheng X, Li J and Wang H-M 2017 *Mater. Des.* **130** 197–207
[6]   Zhang D, Qiu D, Gibson M A, Zheng Y, Fraser H L, StJohn D H and Easton M A 2019 *Nature* **576** 91–5
[7]   Li X P *et al.* 2017 *Acta Mater.* **129** 183–93
[8]   Lin T-C, Cao C, Sokoluk M, Jiang L, Wang X, Schoenung J M, Lavernia E J and Li X 2019 *Nat. Commun.* **10** 4124
[9]   Todaro C J *et al.* 2020 *Nat. Commun.* **11** 142
[10]   Ning F, Hu Y, Liu Z, Cong W, Li Y and Wang X 2017 *Procedia Manuf.* **10** 771–8
[11]   Bermingham M J, StJohn D H, Krynen J, Tedman-Jones S and Dargusch M S 2019 *Acta Mater.* **168** 261–74
[12]   StJohn D H, Qian M, Easton M A and Cao P 2011 *Acta Mater.* **59** 4907–21
[13]   Prasad A, Yuan L, Lee P D and StJohn D H 2013 *Acta Mater.* **61** 5914–27
[14]   Hunt J D 1984 *Mater. Sci. Eng.* **65** 75–83
[15]   Acharya R, Bansal R, Gambone J J and Das S 2014 *Metall. Mater. Trans. B* **45** 2279–90
[16]   Gäumann M, Bezençon C, Canalis P and Kurz W 2001 *Acta Mater.* **49** 1051–62
[17]   Dye D, Hunziker O and Reed R C 2001 *Acta Mater.* **49** 683–97
[18]   Rosenthal D 1941 *Weld. J.* **20** 220–34
[19]   Yuan L and Lee P D 2012 *Acta Mater.* **60** 4917–26
[20]   Yuan L and Lee P D 2010 *Model. Simul. Mater. Sci. Eng.* **18** 55008
[21]   Wang W, Lee P D and McLean M 2003 *Acta Mater.* **51** 2971–87
[22]   Arısoy Y M, Criales L E and Özel T 2019 *Opt. Laser Technol.* **109** 278–92
[23]   Mills K C, Youssef Y M, Li Z and Su Y 2006 *ISIJ Int.* **46** 623–32
[24]   Trivedi R and Kurz W 1994 *Int. Mater. Rev.* **39** 49–74
[25]   Lian Y, Gan Z, Yu C, Kats D, Liu W K and Wagner G J 2019 *Mater. Des.* **169** 107672
[26]   Florian A 1992 *Probabilistic Eng. Mech.* **7** 123–30
[27]   Hann D B, Iammi J and Folkes J 2011 *J. Phys. D. Appl. Phys.* **44** 445401